Flux-pinning-induced stress and strain in superconductors: Case of a long circular cylinder

Tom H. Johansen
Department of Physics, University of Oslo, P.O. Box 1048, Blindern, 0316 Oslo 3, Norway
(Received 23 February 1999)

The irreversible behavior of the flux-pinning-induced stress and strain in a long circular cylindrical superconductor placed in a parallel magnetic field is analyzed. An exact solution of the full three-dimensional (3D) magnetoelastic problem is found. The solution differs from the previous simplified 2D plane stress treatments of the same problem. We derive formulas for all stress and strain components, including the magnetostriction $\Delta R/R$, in terms of the flux density profile in the cylinder. The results are valid for any critical-state model $j_c = j_c(B)$. Based on the Bean model, $j_c = \text{const}$, an extensive analysis is made of the elastic behavior during (1) a complete field cycle after zero-field cooling, and (2) field descent to the remanent state after field cooling. Special emphasis is put on the field-sweep stages generating tensile stresses, which tend to create cracking in the cylinder. A comparison is made between the overall maximum tensile stresses encountered in both processes (1) and (2), which one today uses, e.g., to activate superconducting trapped-field or quasipermanent magnets. [S0163-1829(99)06437-1]

I. INTRODUCTION

Bulk high-temperature superconductors (HTS's) are by increasingly sophisticated preparation methods steadily improving in their flux pinning properties. Of equal importance in this development is that now large-size samples can be prepared free from weak links so that high currents can flow unperturbed throughout the volume, and hence give rise to very large magnetic moments. The material showing today the best combination of these qualities are $(RE)Ba_2Cu_3O_y$ where RE can be one or even several rare-earth elements.[1] A record high critical current density of 6×10^4 A/cm^2 at 77 K and a field of 3 T was recently reported for the ternery compound $(Nd,Eu,Gd)Ba_2Cu_3O_y$ (NEG) with Pt additions.[2] By these improvements the potential has grown considerably for the use of HTS single-domain bulks in a number of applications such as trapped-field magnets and levitating bearings, and one sees today an intensive activity in this direction.[3]

Because the mere size of the HTS is a crucial parameter the magnetic characterization of these materials is often made by recording maps of the field distribution trapped by a full-sized sample. Here one usually measures with a scanning Hall sensor the field near the surface in the remanent state after some initial activation field has been removed. Whereas the figure-of-merit is always the maximum field trapped by the bulk, the field maps can also reveal important information about weak connections between parts of the sample. Quite frequently one finds that internal disconnections, and even complete cracking, are indeed resulting from the activation process itself. Such damaging effects were first studied systematically by Ren *et al.*,[4] who by experiments with field cooling in various fields up to 14 T observed that cracks were created *during* the ramping down of the field. They also explained the cracking tendency by showing that the internal stresses generated by the pinned vortices become tensile and with a maximum magnitude at some point during the field reduction.

A different, but closely related, flux-pinning-induced effect was discovered by Ikuta *et al.*[5] They observed using capacitance dilatometry that superconductors can show a giant magnetostriction, typically of the order of 10^{-5}–10^{-4} when placed in fields of a few Tesla. The observed hysteretic dilatation versus applied field B_a was successfully modeled[5,6] by a formula derived by considering the pinning-induced strain in an infinite slab of half-width w,

$$\Delta w/w = (2c\mu_0 w)^{-1}\int_0^w [B^2(x) - B_a^2]dx. \qquad (1)$$

Here c is an elastic constant and $B(x)$ the local flux density. Later, Johansen and co-workers[7,8] gave an extended and unified critical-state analysis of the two magnetoelastic phenomena for the more realistic geometry of a circular cylinder. Also the case of a square cross section was investigated, showing that the symmetry of the body forces causes here deformations which do not conserve the shape of the cross-sectional area.

In this modeling work the superconductor was assumed to behave magnetically as a long cylinder, so that demagnetization effects can be ignored. At the same time, however, the elasticity problem was analyzed within the plane-stress approximation, which is the scheme normally used to calculate the elastic response of thin plates loaded by forces acting parallel to the plate.

In a fully consistent magnetoelastic treatment of a thick sample the three-dimensional character of the deformation should be accounted for. For this the plane strain scheme is the proper approach.[9] Very recently,[10] the plane strain scheme was applied to find an exact solution of the pinning-induced stress/strain problem for a long rectangular slab in a parallel field. General expressions for all stress and strain components in terms of the flux density distribution were derived. In the present paper we use the same approach for the case of a long circular cylinder. An extensive analysis is given for the various states occurring during a complete cycle of the applied field. Also the decreasing field stage after field cooling is discussed. Special emphasis is put on the stress conditions and probability for cracking during field

reductions ending in the remanent state, i.e., in the process of energizing the HTS to become a quasipermanent, or trapped-field, magnet. The paper is organized as follows.

In Sec. II we first define the magnetoelastic plane strain problem. Then an exact solution is derived for stress and strain in terms of the flux density and elastic constants. In the subsequent sections explicit stress-strain expressions are obtained by assuming a Bean model type of magnetic behavior. Sections III and IV discuss the various states encountered during a complete field cycle. Section V focuses on the external radial magnetostriction $\Delta R/R$. In Section VI the stress-strain picture for field-cooling conditions is presented. Then, in Sec. VII the maximum tensile stress occurring for various field descent routes to the remanent state is discussed, before we finally give the conclusions in Sec. VIII.

II. MAGNETOELASTIC PROBLEM

A. General approach

Consider a type-II superconductor shaped as a circular cylinder and placed in a magnetic field oriented parallel to the cylinder axis (z axis). We seek a solution of the flux-pinning-induced stress-strain problem based on the following assumptions:

(i) The magnetic behavior can be described by the critical-state model. The critical current density can have any dependence on the local induction $j_c = j_c(B)$.

(ii) Demagnetization effects are neglected, i.e., the sample is assumed sufficiently thick to be treated as an infinite cylinder.

(iii) Perpendicular to the cylinder axis the magnetic properties are isotropic.

(iv) Elastically, the cylinder is isotropic, and it has a free surface, i.e., all stresses vanish at the surface.

(v) The deformations are well below the fracture limit thus allowing linear elasticity theory to be applicable.

Under these conditions the sample will in a general magnetized state contain an axially symmetric flux density distribution $B(r)$ and an azimuthal current density satisfying $j_\theta(r) = -B'(r)/\mu_0$. In the critical-state the Lorentz force $j_\theta B$ acting on the vortices is balanced by a distribution of pinning forces. As the pinning forces react back on the crystal lattice the cylinder experiences a radial body force equal to

$$f = -\frac{1}{2\mu_0}\frac{d}{dr}(B^2) \tag{2}$$

per unit volume. Loaded by this axially symmetric and z-independent body force, the free-standing cylinder will deform by radial displacements as well as strain in the longitudinal direction. The elastic response is most conveniently calculated in two steps:

As step 1, let the cylinder be constrained to a fixed length by two rigid and smooth parallel planes allowing the end faces to expand and contract freely in the radial direction, see Fig. 1(a). In this way an axial displacement is prevented and all cross sections are in the same condition. The deformation is then described by a radial displacement $u = u(r)$, and there are only two nonvanishing strain components:

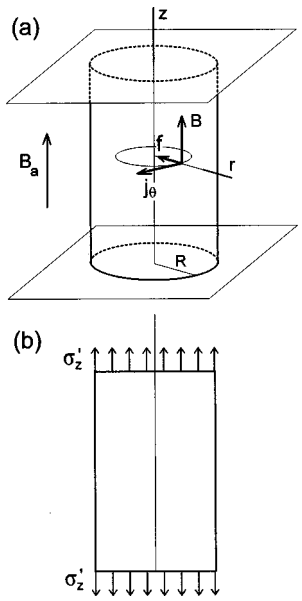

FIG. 1. Long cylindrical superconductor placed in a parallel applied magnetic field B_a. The elastic response to the flux-pinning-induced body forces $f = j_\theta B$ is considered as a superposition of two deformations. (a) First, the forces create a purely radial displacement in the cylinder which is thought to be confined between two perfectly smooth and rigid planes. (b) Second, the condition of free surfaces is recovered by letting the averaged axial stress $\langle \sigma_z \rangle$ built up in (a) be compensated by adding the opposite stress σ_z' distributed uniformly over the end faces of the cylinder.

$$e_r = u'(r) \quad \text{and} \quad e_\theta = u/r, \tag{3}$$

the radial and tangential (hoop) strain, respectively. The relations between the strains e_r, e_θ, e_z and the corresponding stresses $\sigma_r, \sigma_\theta, \sigma_z$ are

$$\begin{aligned} E e_r &= \sigma_r - \nu(\sigma_\theta + \sigma_z), \\ E e_\theta &= \sigma_\theta - \nu(\sigma_z + \sigma_r), \\ E e_z &= \sigma_z - \nu(\sigma_r + \sigma_\theta), \end{aligned} \tag{4}$$

where E and ν is the Young's modulus and Poisson's ratio, respectively. Because of the constraint $e_z = 0$, there will be a buildup of axial stress σ_z, amounting to $\sigma_z = \nu(\sigma_r + \sigma_\theta)$, which may be compressive or tensile.

As step 2, in order to recover the condition of free end faces, we add a uniform axial stress, see Fig. 1(b), of magnitude:

$$\langle \sigma_z \rangle = R^{-2} \int_0^R \sigma_z(r) 2r\,dr, \tag{5}$$

which is the cross-sectional average of $\sigma_z(r)$ found under step 1. The second stress is applied opposite to the built-up stress, i.e., if the constraint gave a compressive $\langle \sigma_z \rangle$ the added stress is tensile, and vice versa. This superposition results in a zero net axial stress in the cylinder. According to Saint-Venant's principle the procedure gives the correct resultant elastic state except for local deviations close to the cylinder's end faces.[9]

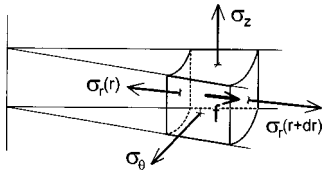

FIG. 2. Volume element of a cylinder loaded by an axially symmetric body force distribution f. When conditions are the same at all cross sections, as during the deformation step 1 [Fig. 1(a)], it is sufficient to consider only a slice of the cylinder. Indicated are the nonzero stress components.

B. Cylinder of fixed length

We determine first the elastic response of the cylinder subjected to the body force, Eq. (2), and constrained by the condition $e_z=0$. It follows that the stress-strain relations then become

$$e_r=\frac{1+\nu}{E}[(1-\nu)\sigma_r-\nu\sigma_\theta],$$

$$e_\theta=\frac{1+\nu}{E}[(1-\nu)\sigma_\theta-\nu\sigma_r], \tag{6}$$

and conversely,

$$\sigma_r=\frac{E}{1-\nu-2\nu^2}[(1-\nu)e_r+\nu e_\theta],$$

$$\sigma_\theta=\frac{E}{1-\nu-2\nu^2}[(1-\nu)e_\theta+\nu e_r],$$

$$\sigma_z=\frac{\nu E}{1-\nu-2\nu^2}(e_r+e_\theta). \tag{7}$$

The stresses acting on a volume element are illustrated in Fig. 2. The condition of static equilibrium in the radial direction is

$$\sigma_r'(r)+\frac{\sigma_r-\sigma_\theta}{r}+f=0. \tag{8}$$

Using Eqs. (3) and (7) this can be expressed in terms of the displacement field as

$$u''+\frac{1}{r}u'-\frac{1}{r^2}u+\frac{1-\nu-2\nu^2}{(1-\nu)E}f=0. \tag{9}$$

The corresponding equation valid for the plane stress approximation deviates only by having a different prefactor in the body force term.[8] Since Eq. (9) can be written as

$$\frac{d}{dr}\left[\frac{1}{r}\frac{d(ru)}{dr}\right]=\frac{1-\nu-2\nu^2}{2(1-\nu)E\mu_0}\frac{d}{dr}(B^2); \tag{10}$$

it allows twice integration, which gives

$$u(r)=\frac{1-\nu-2\nu^2}{2(1-\nu)E\mu_0}r\left[\frac{1}{r^2}\int_0^r r'B^2dr'+\frac{1-2\nu}{R^2}\times\int_0^R r'B^2dr'-(1-\nu)B_a^2\right]. \tag{11}$$

Here two integration constants were determined from the free-surface condition $\sigma_r(r=R)=0$, and using that $u_r(0)=0$. From this formula for $u(r)$ one can calculate the complete stress-strain picture produced by a given flux density distribution $B(r)$. For the stresses, Eq. (7), we find

$$\sigma_r(\rho)=\frac{1}{2\mu_0}\left[B^2-B_a^2+\frac{1-2\nu}{1-\nu}\times\left(\int_0^1\rho'B^2d\rho'-\frac{1}{\rho^2}\int_0^\rho\rho'B^2d\rho'\right)\right], \tag{12}$$

$$\sigma_\theta(\rho)=\frac{1}{2\mu_0}\left[\frac{\nu}{1-\nu}B^2-B_a^2+\frac{1-2\nu}{1-\nu}\times\left(\int_0^1\rho'B^2d\rho'+\frac{1}{\rho^2}\int_0^\rho\rho'B^2d\rho'\right)\right], \tag{13}$$

and

$$\sigma_z(\rho)=\frac{1}{2\mu_0}\left(\frac{\nu}{1-\nu}B^2-2\nu B_a^2+2\nu\frac{1-2\nu}{1-\nu}\int_0^1\rho'B^2d\rho'\right), \tag{14}$$

where $\rho\equiv r/R$. The stresses are evidently not uniformly distributed in the cylinder. This applies even for the axial stress, which in fact has the same spatial variation as that of $B(r)^2$. From Eqs. (6), (12), and (13) one finds the strains e_r and e_θ in the constrained state. Note that the last integral term in Eqs. (12) and (13) approaches the value $B(0)^2/2$ as $\rho\to0$, and that this implies $\sigma_r(0)=\sigma_\theta(0)$.

C. Recovering free ends

To recover the condition of free end faces the built-up axial stress, Eq. (14), is compensated by applying externally the uniform stress $\sigma_z'=-\langle\sigma_z\rangle$, which from Eq. (5) becomes

$$\sigma_z'=\frac{2\nu}{\mu_0}\int_0^1\rho(B_a^2-B^2)d\rho. \tag{15}$$

This modifies the strains as follows. To both e_r and e_θ the term $-\nu\sigma_z'/E$ is added, or equivalently, the displacement $u(r)$ receives an extra term $-\nu\sigma_z'r/E$. From Eq. (11) one then obtains the final expression

$$u(\rho)=\frac{1-\nu}{2E\mu_0}\rho R\left[\frac{1-\nu-2\nu^2}{(1-\nu)^2\rho^2}\int_0^\rho\rho'B^2d\rho'+\frac{1-3\nu+4\nu^2}{(1-\nu)^2}\int_0^1\rho'B^2d\rho'-B_a^2\right]. \tag{16}$$

Of particular interest is the observable external dilatation $\Delta R=u(1)$, which takes the simple form

$$\frac{\Delta R}{R}=-\frac{1-\nu}{E\mu_0}\int_0^1\rho(B_a^2-B^2)d\rho. \tag{17}$$

Interestingly, this formula is the same as derived earlier[7] in the plane stress approximation. The expression for $u(\rho)$, however, is different, as are the results for strains and stresses.

The final formula for the radial strain becomes

$$e_r(\rho)=\frac{1-\nu}{2E\mu_0}\left[\frac{1-\nu-2\nu^2}{(1-\nu)^2}\left(B^2-\frac{1}{\rho^2}\int_0^\rho \rho' B^2 d\rho'\right)+\frac{1-3\nu+4\nu^2}{(1-\nu)^2}\int_0^1 \rho' B^2 d\rho' - B_a^2\right], \tag{18}$$

while the final hoop strain

$$e_\theta(\rho)=u(\rho)/\rho R \tag{19}$$

follows directly from Eq. (16). The compensating stress, Eq. (15), generates also a longitudinal deformation of the cylinder. This is described by a uniform axial strain equal to $e_z=\sigma_z'/E$, which can be expressed as

$$e_z=-\frac{2\nu}{1-\nu}\frac{\Delta R}{R}. \tag{20}$$

The superposition of the uniform axial stress, σ_z' does not influence the other two stress components. Hence the expressions Eqs. (12) and (13) for σ_r and σ_θ remain valid.

D. Flux density profiles and notation

In order to calculate explicit expressions for stress and strain one needs first to determine the flux density profiles $B(\rho)$ for the various stages of a magnetization process. Given the appropriate function $j_c(B)$ this can be done by integrating

$$d\rho=-\frac{1}{\mu_0 R}\frac{dB}{j_\theta(B)}, \tag{21}$$

where $j_\theta(B)$ has the magnitude of $j_c(B)$, and a sign in accordance with the magnetic history as prescribed by the critical-state model. In this paper we restrict the calculations to the Bean model, i.e., $j_c(B)=\text{const}$, which leads to linear or piecewise linear profiles $B(\rho)$.

We consider first a superconductor initially zero-field cooled below T_c, followed by a complete cycle of the applied field B_a. The maximum applied field, which we denote by $\hat{B}_a$, is assumed larger than, or equal to, the full penetration field, which for the Bean model equals $B_p=\mu_0 j_c R$. When $\hat{B}_a \geqslant 2B_p$ the magnetization process is one that gives a maximum trapped field in the subsequent remanent state. In the sections below both of the cases, $\hat{B}_a$ larger and smaller than $2B_p$, will be discussed in detail. To simplify notation, we normalize all magnetic fields by B_p, and write $b\equiv B/B_p, b_a\equiv B_a/B_p$, etc. The parameters defined by

$$\sigma_0\equiv\frac{B_p^2}{2\mu_0} \quad \text{and} \quad e_0\equiv\frac{B_p^2}{E\mu_0}, \tag{22}$$

will appear as prefactors in the expressions for stress and strain, respectively.

III. INCREASING FIELD

A. Stage 1, $B_a<B_p$

Starting with a flux free superconductor an increasing applied field causes flux to penetrate into the cylinder in an outer shell of thickness b_a, i.e., the flux front is located at $\rho=a$ where

$$a=1-b_a. \tag{23}$$

During this virgin magnetization the flux density is given by $b=b_a+\rho-1$ for $a\leqslant\rho<1$, and by $b=0$ for $\rho<a$. The two regions require separate calculations, and Eqs. (12), (13), (18), and (19) yield for $0\leqslant\rho<a$:

$$\sigma_r=\sigma_\theta=-\sigma_0\left(b_a^2+\frac{1-2\nu}{1-\nu}\frac{b_a-4}{12}b_a^3\right), \tag{24}$$

$$e_r=e_\theta=-e_0\left(\frac{1-\nu}{2}b_a^2+\frac{1-3\nu+4\nu^2}{1-\nu}\frac{b_a-4}{24}b_a^3\right), \tag{25}$$

and for $a\leqslant\rho\leqslant 1$:

$$\frac{\sigma_r}{\sigma_0}=(b_a+\rho-1)^2-b_a^2+\frac{1-2\nu}{1-\nu}\times\left[\frac{b_a-3\rho-1}{12\rho^2}(b_a+\rho-1)^3-\frac{b_a-4}{12}b_a^3\right], \tag{26}$$

$$\frac{\sigma_\theta}{\sigma_0}=\frac{\nu}{1-\nu}(b_a+\rho-1)^2-b_a^2-\frac{1-2\nu}{1-\nu}\times\left[\frac{b_a-3\rho-1}{12\rho^2}(b_a+\rho-1)^3+\frac{b_a-4}{12}b_a^3\right], \tag{27}$$

$$\frac{e_r}{e_0}=\frac{1-\nu-2\nu^2}{1-\nu}\left[\frac{4\rho-3}{6}(b_a-1)+\frac{3\rho^2-2}{8}+\frac{(b_a-1)^4}{24\rho^2}\right]-\frac{1-3\nu+4\nu^2}{1-\nu}\frac{b_a^2-4b_a+6}{24}b_a^2, \tag{28}$$

$$\frac{e_\theta}{e_0}=\frac{1-\nu-2\nu^2}{1-\nu}\frac{3\rho-b_a+1}{24\rho^2}(b_a+\rho-1)^3-\frac{1-3\nu+4\nu^2}{1-\nu}\frac{b_a-4}{24}b_a^3-\frac{1-\nu}{2}b_a^2. \tag{29}$$

Figure 3 shows the stress distributions in the cylinder for four values of the increasing applied field. Both stress components are negative, i.e., compressive, and increase in magnitude towards the center. In the nonpenetrated inner region $\rho<a$, where the body forces are zero, the stresses are uniform. The position of the flux front for various b_a is indicated in the graphs as a dashed line. For small applied fields the stresses grow relatively slowly, proportional to b_a^2. Note that the two stress components differ in the way they decrease towards the surface. Whereas σ_r falls to zero at $\rho=1$, as dictated by the free-surface condition, the hoop stress decreases to a finite value at the surface. In this figure, as in all other graphs presented in the paper, a Poisson ratio equal to $\nu=0.3$ is chosen.[4,11]

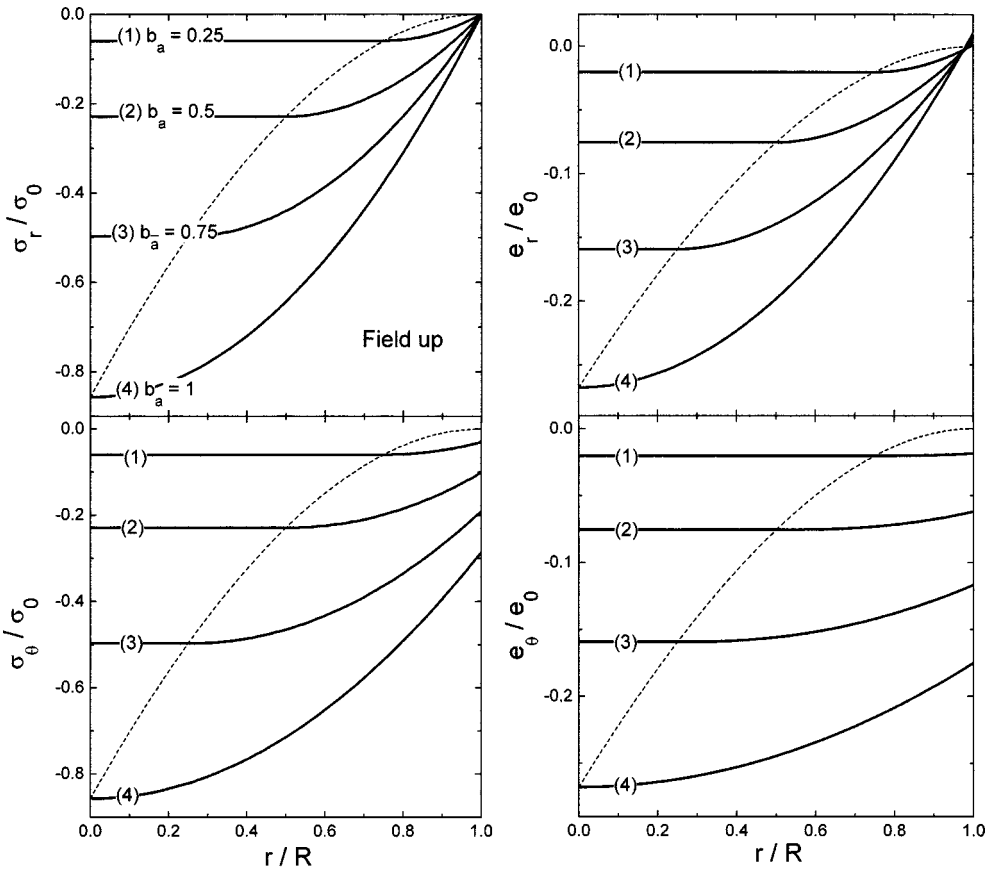

FIG. 3. Distribution of radial (upper) and hoop (lower) stress and strain as the applied field is increased from zero and up until a state of full flux penetration is reached. The indicated values of the field b_a are given relative to the full penetration field $B_p=\mu_0 j_c R$. The curves are labeled (1)–(4) in a consistent way. The dashed lines represent the position of the flux front as the field increases.

The strain components e_r and e_θ are also shown in Fig. 3. The strain distributions behave quite similarly to the corresponding stresses. Note, however, that e_r does not reduce to exactly zero at the surface, but crosses over to a small positive value at ρ just below 1. This means that an expansive radial strain occurs in the outermost layer while the cylinder is loaded by only compressive forces. This surprising result can in fact be seen directly from Eqs. (18) and (19), which when evaluated at $\rho=1$ give the following two relations of general validity:

$$e_r(1)=\nu\frac{3\nu-1}{(1-\nu)^2}\frac{\Delta R}{R} \quad \text{and} \quad e_\theta(1)=\frac{\Delta R}{R}. \tag{30}$$

Hence near the surface the two strains will always have opposite signs if $\nu<\frac{1}{3}$, as here.

B. Stage 2, $B_a \geqslant B_p$

As the field is increased above the full penetration value, the critical current fills the entire cylinder, and the flux density is given by $b=b_a+\rho-1$ for all ρ. The evaluation of the elastic response now yields

$$\frac{\sigma_r}{\sigma_0}=\left[\frac{3-2\nu}{1-\nu}\frac{\rho}{4}+\frac{2-\nu}{1-\nu}\frac{2b_a}{3}-\frac{7-2\nu}{12(1-\nu)}\right](\rho-1), \tag{31}$$

$$\frac{\sigma_\theta}{\sigma_0}=\frac{1+2\nu}{1-\nu}\frac{\rho^2}{4}+2\frac{1+\nu}{1-\nu}\frac{b_a-1}{3}\rho-\frac{2-\nu}{1-\nu}\frac{2b_a}{3}+\frac{7-2\nu}{12(1-\nu)}, \tag{32}$$

$$\frac{e_r}{e_0}=\frac{1-\nu-2\nu^2}{1-\nu}\left(\frac{3\rho}{8}+2\frac{b_a-1}{3}\right)\rho-\frac{2-3\nu-\nu^2}{1-\nu}\frac{b_a}{3}+\frac{7-9\nu-8\nu^2}{24(1-\nu)}, \tag{33}$$

$$\frac{e_\theta}{e_0}=\frac{1-\nu-2\nu^2}{1-\nu}\left(\frac{\rho}{8}+\frac{b_a-1}{3}\right)\rho-\frac{2-3\nu-\nu^2}{1-\nu}\frac{b_a}{3}+\frac{7-9\nu-8\nu^2}{24(1-\nu)}. \tag{34}$$

Figure 4 shows the stress-strain picture for applied fields up to $b_a=4$. Above the full penetration field both stress and strain at a given point ρ grow in magnitude linearly with the applied field. As b_a becomes large all the profiles, which are parabolic in ρ, will approach straight lines. The slope in the σ_r profile is then a factor $(2-\nu)/(1+\nu)$ larger than for σ_θ, whereas the slope of $e_r(\rho)$ is twice that of $e_\theta(\rho)$, independently of ν. Provided that $\nu\leqslant\frac{1}{3}$, the point where the radial strain changes sign approaches $\rho=1-(\nu-3\nu^2)/(2-2\nu-4\nu^2)$.

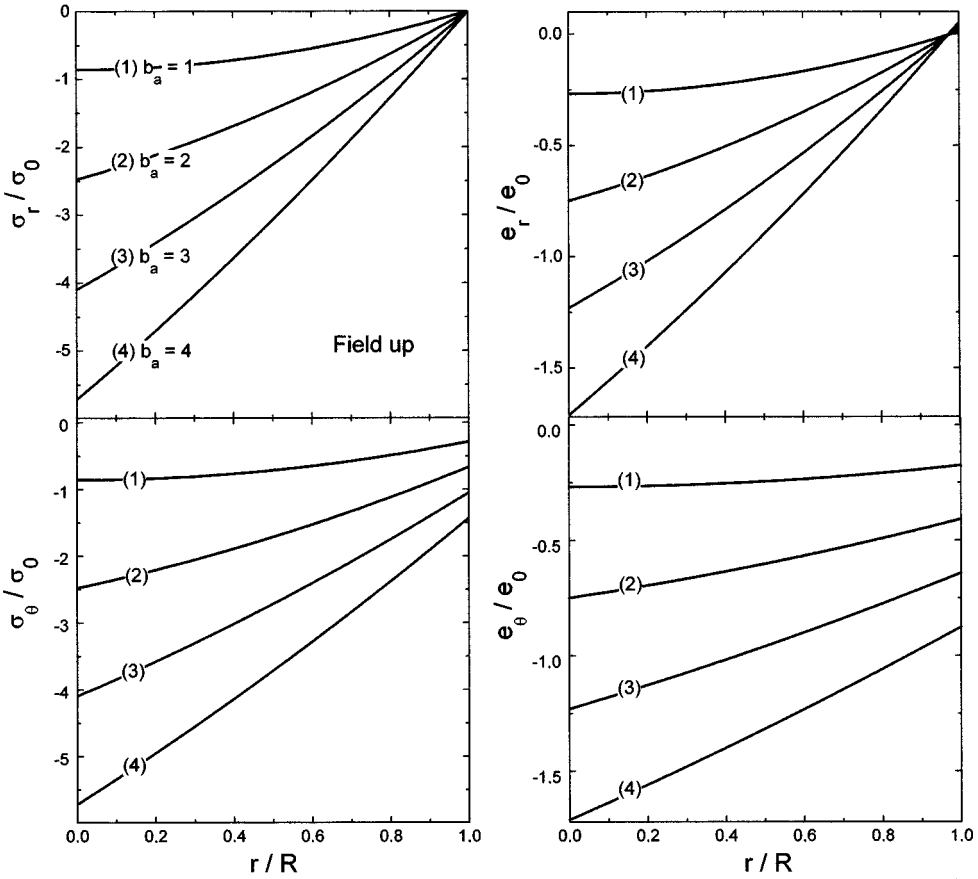

FIG. 4. Radial (upper) and hoop (lower) stress and strain in the cylinder as B_a is increased above B_p.

IV. DECREASING FIELD

A. Stage 1, $\hat{B}_a - 2B_p < B_a < \hat{B}_a$

When the applied field decreases from its maximum value $\hat{b}_a$, the direction of the critical current is reversed in the outer part of the cylinder. In this remagnetized region the body forces now point away from the symmetry axis, whereas the forces remain unchanged in the inner part. Therefore during the field reduction, where both compressive and expansive forces are simultaneously present, the distributions of stress and strain will vary dramatically along a radius. From the Bean model it follows that the remagnetization front is located at

$$\rho_0 = 1 - \frac{\hat{b}_a - b_a}{2}. \tag{35}$$

The current becomes reversed throughout the volume first when b_a is reduced by twice the full penetration field. We consider in this section only the stage of incomplete current reversal, i.e., as ρ_0 decreases from 1 to 0.

To calculate stress and strain from Eqs. (12), (13), (18), and (19) we now use that in the inner part, $0 \leqslant \rho < \rho_0$, the flux density is given by $b_{(i)} = \hat{b}_a + \rho - 1$. In the remagnetized region, $\rho_0 \leqslant \rho \leqslant 1$ the flux density equals $b_{(o)} = b_a + 1 - \rho$. Again the two parts of the cylinder require separate calculations, and we find for $0 \leqslant \rho < \rho_0$:

$$\frac{\sigma_r}{\sigma_0} = (\hat{b}_a + \rho - 1)^2 - b_a^2 + \frac{1-2\nu}{1-\nu}\left[\frac{\hat{b}_a + b_a}{24}(\hat{b}_a - b_a - 6) \times (\hat{b}_a - b_a)^2 + \frac{3\rho + 8\hat{b}_a - 5}{12}(1-\rho)\right], \tag{36}$$

$$\frac{\sigma_\theta}{\sigma_0} = \frac{(3+6\nu)\rho^2 - 8(1+\nu)(1-\hat{b}_a)\rho - 8(2-\nu)\hat{b}_a + 7 - 2\nu}{12(1-\nu)} + (\hat{b}_a^2 - b_a^2)\left[1 + \frac{1-2\nu}{1-\nu}\frac{\hat{b}_a - b_a}{24}(\hat{b}_a - b_a - 6)\right], \tag{37}$$

$$\frac{e_r}{e_0} = \frac{1-\nu-2\nu^2}{2(1-\nu)}\left[b_{(i)}^2 - \frac{1}{\rho^2}\int_0^\rho \rho' b_{(i)}^2 d\rho'\right] + \frac{1-3\nu+4\nu^2}{2(1-\nu)} \times \left[\int_0^{\rho_0} \rho b_{(i)}^2 d\rho + \int_{\rho_0}^1 \rho b_{(o)}^2 d\rho\right] - \frac{1-\nu}{2} b_a^2, \tag{38}$$

$$\frac{e_\theta}{e_0} = \frac{1-\nu-2\nu^2}{2(1-\nu)\rho^2}\int_0^\rho \rho' b_{(i)}^2 d\rho' + \frac{1-3\nu+4\nu^2}{2(1-\nu)} \times \left[\int_0^{\rho_0} \rho b_{(i)}^2 d\rho + \int_{\rho_0}^1 \rho b_{(o)}^2 d\rho\right] - \frac{1-\nu}{2} b_a^2, \tag{39}$$

and for $\rho_0 \leqslant \rho \leqslant 1$:

$$\frac{\sigma_r}{\sigma_0}=(1-\rho)\left\{2b_a+1-\rho+\frac{1-2\nu}{1-\nu}\times\left[\frac{\hat{b}_a+b_a}{24}(2+b_a-\hat{b}_a)^3\frac{1+\rho}{\rho^2}+\frac{3\rho-8b_a-5}{12}\right]\right\}, \tag{40}$$

$$\frac{\sigma_\theta}{\sigma_0}=\frac{(3+6\nu)\rho^2-8(1+\nu)(1+b_a)\rho+8(2-\nu)\hat{b}_a+7-2\nu}{12(1-\nu)}+\frac{1-2\nu}{1-\nu}\frac{\hat{b}_a+b_a}{24}(\hat{b}_a-b_a-2)^3\left(1+\frac{1}{\rho^2}\right), \tag{41}$$

$$\frac{e_r}{e_0}=\frac{1-\nu-2\nu^2}{2(1-\nu)}\left[b_{(o)}^2-\frac{1}{\rho^2}\int_0^{\rho_0}\rho b_{(i)}^2d\rho-\frac{1}{\rho^2}\int_{\rho_0}^{\rho}\rho' b_{(o)}^2d\rho'\right]+\frac{1-3\nu+4\nu^2}{2(1-\nu)}\left[\int_0^{\rho_0}\rho b_{(i)}^2d\rho+\int_{\rho_0}^{1}\rho b_{(o)}^2d\rho\right]-\frac{1-\nu}{2}b_a^2, \tag{42}$$

$$\frac{e_\theta}{e_0}=\frac{1-\nu-2\nu^2}{2(1-\nu)\rho^2}\left[\int_0^{\rho_0}\rho b_{(i)}^2d\rho+\int_{\rho_0}^{\rho}\rho' b_{(o)}^2d\rho'\right]+\frac{1-3\nu+4\nu^2}{2(1-\nu)}\left[\int_0^{\rho_0}\rho b_{(i)}^2d\rho+\int_{\rho_0}^{1}\rho b_{(o)}^2d\rho\right]-\frac{1-\nu}{2}b_a^2. \tag{43}$$

The strains are listed as integral expressions to show how the calculations are carried out when the flux profile consists of two segments. The integration itself is straightforward. Note that during the field descent one may or may not, depending on $\hat{b}_a$, pass through the remanent state $b_a=0$. In any case, the formulas Eqs. (36)–(43) are valid. We will now look in detail on the remagnetization process starting from three selected $\hat{b}_a$, see Fig. 5, all giving qualitatively different stress-strain behaviors.

Case (i): $\hat{B}_a=4B_p$

Figure 6 shows the stress distributions while the applied field is reduced from $\hat{b}_a=4$ to $b_a=2$, i.e., the starting condition is given by the set of curves labeled (4) in Fig. 4. The radial stress begins immediately to become tensile in the outer part of the cylinder. A sequence of cusped peaks accompany the motion of the remagnetization front $\rho_0(b_a)$, the point where also the flux density is maximum. Note that the region of tensile σ_r is about twice as wide as the entire remagnetized region. Hence below $b_a\simeq\hat{b}_a-1$ the radial stress becomes tensile throughout.

The hoop stress behaves differently, as σ_θ remains everywhere compressive until b_a is reduced by approximately 0.3. Then, tension first occurs in the cylinder at $\rho\simeq0.85$. Like $\sigma_r(\rho)$, also $\sigma_\theta(\rho)$ has a cusped maximum at the remagnetization front, although the peak in σ_θ is less sharp.

Tensile stresses tend to generate cracks, or expand already existing microcracks in the material. Hence the behavior of the maxima in σ_r and σ_θ give crucial information about the probability for cracking in the tangential and radial directions, respectively. It is readily derived that the envelope curve for the two stress peaks are given by

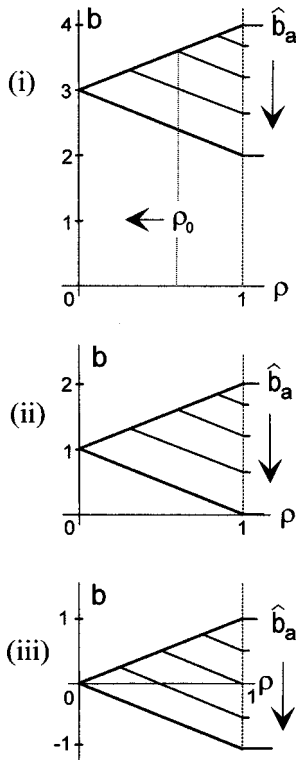

FIG. 5. Remagnetization as the applied field is reduced from three different maximum values $\hat{b}_a$, where in (i) $\hat{b}_a=4$, (ii) $\hat{b}_a=2$, and in (iii) $\hat{b}_a=1$. Shown are the flux density profiles as b_a decreases until the current is reversed in all the cylinder volume.

$$\frac{\sigma_r^{\max}}{\sigma_0}=\left[\frac{1-2\nu}{1-\nu}\frac{8\rho^3+8(\rho^2+\rho-1)\hat{b}_a-21\rho+11}{12}+3\rho+2\hat{b}_a-3\right](1-\rho), \tag{44}$$

$$\frac{\sigma_\theta^{\max}}{\sigma_0}=2\frac{1-2\nu}{1-\nu}\frac{1-\rho-\hat{b}_a}{3}\rho^3-\frac{7-2\nu}{1-\nu}\frac{\rho^2}{4}+2\frac{2-\nu}{1-\nu}\frac{3\rho+(1-\rho)\hat{b}_a}{3}-\frac{25-14\nu}{12(1-\nu)}, \tag{45}$$

for field reductions from any $\hat{b}_a\geqslant1$. In Figs. 6, 7, and 8 the peak envelopes are plotted as dashed curves.

For the present case, $\hat{b}_a=4$, both envelope curves are seen to be monotoneous. The stresses have therefore a common overall maximum, $\sigma^{\max}=4\sigma_0$, at $\rho=0$, which occurs when the current reversal is completed. Hence during this remagnetization process the last stage is the most critical, and cracking is most likely to be initiated in the center of the cylinder.

Shown in Fig. 6 is also the behavior of the strains e_r and e_θ for the same sequence of decreasing fields. Except very close to the surface, the curves for the radial strain follow closely the behavior of the radial stress. The hoop strain curves, on the other hand, contrast all the others by lacking the peak at the remagnetization front. In fact, one has to

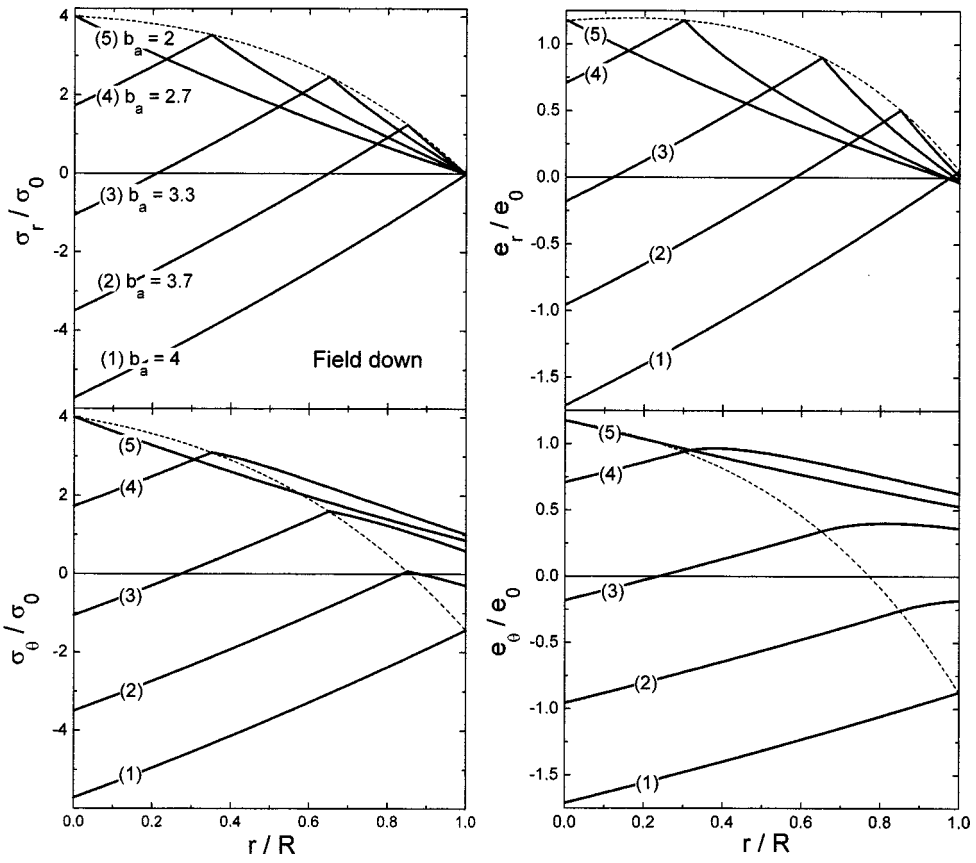

FIG. 6. Stress and strain distributions as the field is reduced from $\hat{b}_a=4$ to $b_a=2$, see Fig. 5(i). The dashed lines show the stress and strain at the remagnetization front, and forms also the envelope curve for maximum local stress and radial strain as b_a is decreased. For e_θ the dashed curve is *not* the envelope of local maximum. Positive stress values correspond to tension.

reduce the field considerably before a peak appears at all. Eventually, a broad maximum in e_θ occurs at some $\rho>\rho_0$, which finally ends up at $\rho=0$. The dashed curves plotted together with the e_r and e_θ graphs show the strain at ρ_0.

Case (ii): $\hat{B}_a=2B_p$

Figure 7 illustrates the behavior of σ_r, σ_θ, e_r, and e_θ, as the applied field is reduced from $\hat{b}_a=2$ to $b_a=0$. This is the activation process giving maximum trapped flux in the remanent state at a minimum cost in terms of applied field (field-cooling processes are discussed later). The starting condition is now given by the set of curves (2) in Fig. 4.

The most striking difference from the previous case (i) is that stress and strain maxima now follow nonmonotoneous paths towards the remanent state. All the global maxima have moved away from the cylinder axis, namely to $\rho=0.42$, 0.32, 0.49, and 0.40 for σ_r, σ_θ, e_r, and e_θ, respectively. Highest cracking probability is therefore now in positions far from the center. We also find that the maximum radial stress and strain are both larger than their hoop counterparts. Hence tangentially oriented cracks are the more likely to be initiated or expanded. On the other hand, if tangential cracks do not grow too large in size their effect on the final trapped field will not be significant since the circular flow of the persistent current is only weakly perturbed. In this respect the formation of cracks running radially are by far more deteriorating, as illustrated in Fig. 8(a).

Another remarkable difference is that stress and strain magnitudes are substantially reduced relative to the $\hat{b}_a=4$ case. In particular, all maxima are nearly a factor of 4 lower. Therefore in energizing a trapped-field magnet a maximum field $\hat{b}_a$ larger than 2 should from a mechanical point of view be avoided. In practice, however, this is not easily realized as the full penetration field of the superconductor is usually not known in advance.

The fact that highest cracking probability is now found at large ρ is not favorable. Destroying current loops of large area rapidly reduces the remanent magnetic moment as compared to losing currents near the center. As shown schematically in Fig. 8(b), a defect near the axis only cuts off a small top part of the ''flux density cone,'' whereas defects far from the axis easily reduces the width of the entire cone representing the trapped field. Note, however, that the maximum value itself is not so sensitive to the position of the defected region. Of course, fully realistic considerations concerning cracking probabilities can not be carried out unless stress concentrations are correlated with the mechanical homogeneity of the grown superconducting sample.

Case (iii): $\hat{B}_a=B_p$

Figure 9 shows the stress and strain as the applied field is reduced after being first raised to $\hat{b}_a=1$. In this particular field range, b_a from 1 to -1, the elastic response undergoes a complete cycle. As in the previous case (ii), the global

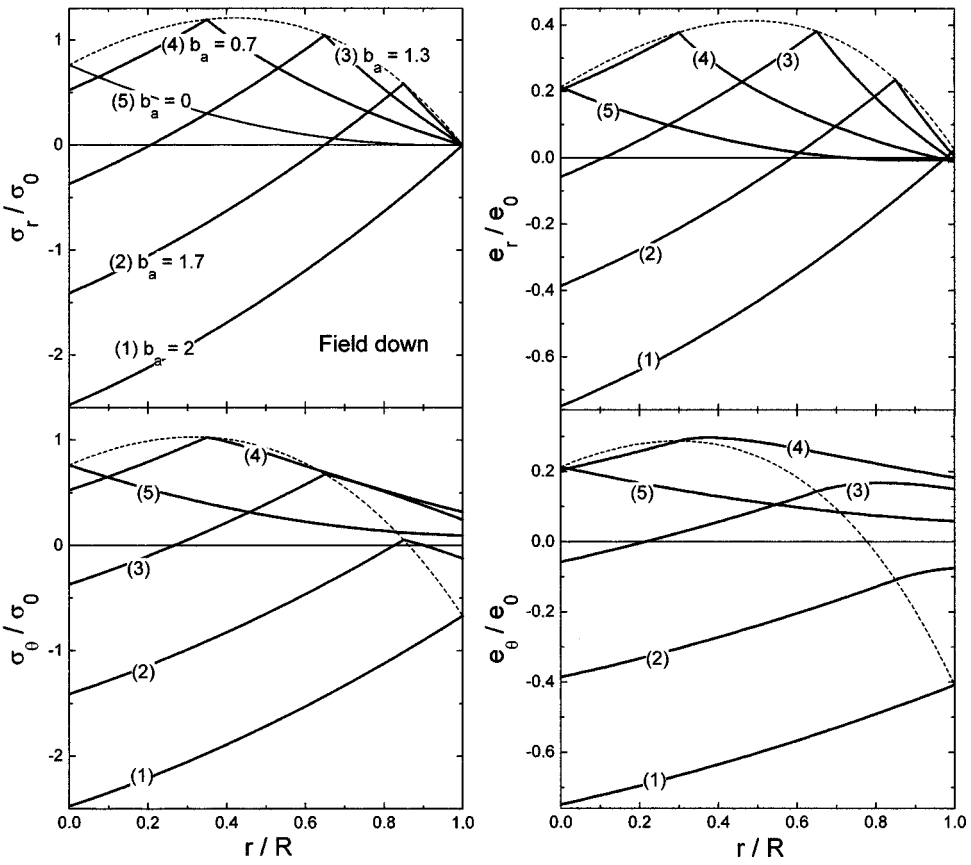

FIG. 7. Stress and strain as the field decreases from $\hat{b}_a=2$ to the remanent state, $b_a=0$, see Fig. 5(ii). See also caption to Fig. 6.

stress and strain maxima occur *before* the remanent state is reached. However, the remanent state itself, represented by the curves labeled (3), is now different as all the cusped maxima are located at $\rho_0=0.5$. The hoop strain has again a broad peak, here centered at $\rho=0.61$. One can, in fact, show quite generally from Eqs. (39) and (43) that the two curve segments making up the $e_\theta(\rho)$ profile always combine at ρ_0 with equal derivatives, hence the smooth hoop strain distribution.

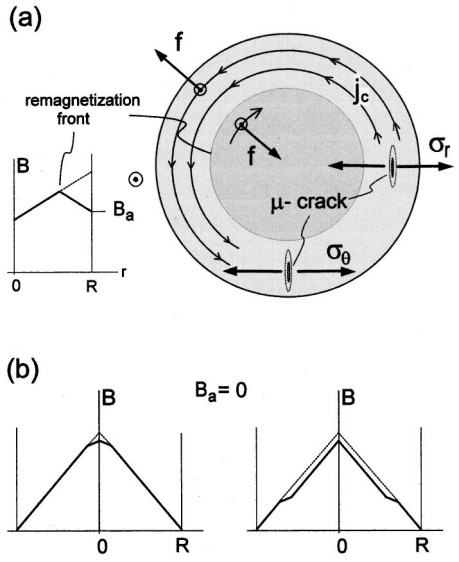

FIG. 8. (a) During field reduction the stresses σ_r and σ_θ become tensile and may generate cracks. Shows are two types of cracks; one tangential—easily expanded by σ_r, and one radial—easily expanded by σ_θ. (b) The cone of trapped field in the remanent state is perturbed differently depending on whether the cracked region is near the center (left case) or at a large radius (right case).

Compared to the previous two cases there is also here large reductions in stress and strain values. In the remanent state the maximum tensile stress is now only $0.24\sigma_0$ and $0.17\sigma_0$ for the radial and hoop component, respectively, whereas with $\hat{b}_a=2$ it amounts to $0.76\sigma_0$ for both components. The strong field dependence of characteristic features in the elastic response are, in fact, to be expected since the general expressions, Eqs. (12)–(20), for stress and strain are all quadratic in the flux density.

The remanent state is also characterized by having zeros in the radial stress and strain, located at $\rho=0.95$ and 0.87, respectively. This feature, however, is very sensitive to the exact value of the Poisson ratio. Actually, the zero in e_r vanishes when $\nu>0.343$, while the same happens for σ_r for ν close to the limiting value 0.5.

B. Stage 2, $B_a \leqslant \hat{B}_a - 2B_p$

When the applied field has been reduced by more than twice the full penetration field the current is reversed in all the cylinder volume, and the flux density is given by $b=b_a+1-\rho$. This yields the following expressions for stress and strain:

$$\frac{\sigma_r}{\sigma_0}=\left[\frac{3-2\nu}{1-\nu}\frac{\rho}{4}-\frac{2-\nu}{1-\nu}\frac{2b_a}{3}-\frac{7-2\nu}{12(1-\nu)}\right](\rho-1), \quad (46)$$

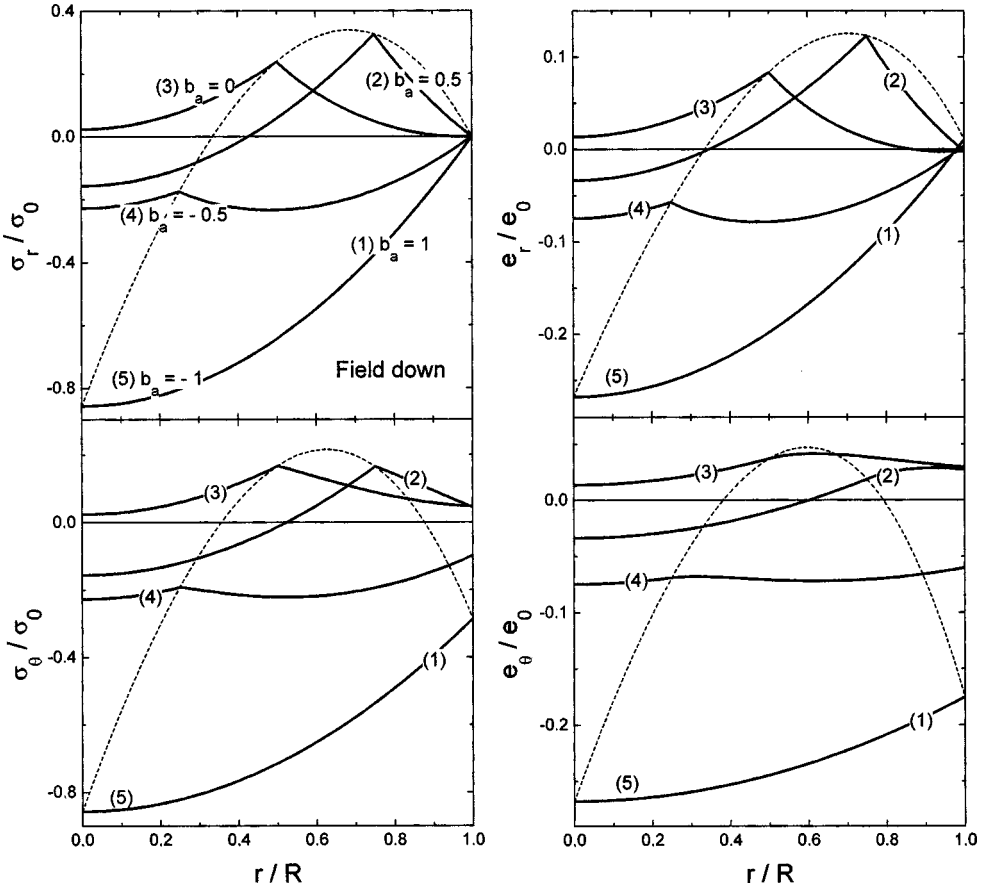

FIG. 9. Stress and strain as the field decreases from $\hat{b}_a=1$ to $b_a=-1$, see Fig. 5(iii). The initial and final state, labeled (1) and (5), have identical stress and strain profiles.

$$\frac{\sigma_\theta}{\sigma_0}=\frac{1+2\nu}{1-\nu}\frac{\rho^2}{4}-2\frac{1+\nu}{1-\nu}\frac{b_a+1}{3}\rho+\frac{2-\nu}{1-\nu}\frac{2b_a}{3}+\frac{7-2\nu}{12(1-\nu)}, \tag{47}$$

$$\frac{e_r}{e_0}=\frac{1-\nu-2\nu^2}{1-\nu}\left(\frac{3\rho}{8}-2\frac{b_a+1}{3}\right)\rho + \frac{2-3\nu-\nu^2}{1-\nu}\frac{b_a}{3}+\frac{7-9\nu-8\nu^2}{24(1-\nu)}, \tag{48}$$

$$\frac{e_\theta}{e_0}=\frac{1-\nu-2\nu^2}{1-\nu}\left(\frac{\rho}{8}-\frac{b_a+1}{3}\right)\rho + \frac{2-3\nu-\nu^2}{1-\nu}\frac{b_a}{3}+\frac{7-9\nu-8\nu^2}{24(1-\nu)}. \tag{49}$$

As an example, Fig. 10 shows the elastic behavior as b_a is reduced from 2 to -1, i.e., it is assumed that the field had previously been raised to $\hat{b}_a=4$ or larger. During field reduction towards $b_a=0$ the stresses are tensile, and with maxima always in the cylinder center. Both strain components behave again similarly to the stress components. Note in the remanent state that both σ_r and e_r also now have zeros, as seen more clearly in the figure inserts.

Decreasing the field below $b_a=0$ one gradually reaches at $b_a=-1$ the same elastic state as at full virgin penetration $b_a=1$, i.e., the curves labeled (4) in Fig. 10 are identical to the curves labeled (4) in Fig. 3. If b_a is reduced even more one only reproduces for $b_a<-1$ the stress-strain behavior already described for increasing fields $b_a>1$. This symmetry between states at opposite fields $\pm b_a$ is quite general, and follows from the fact that the body force equals the product of current and flux density, which both have opposite sign but are otherwise equally distributed at $\pm b_a$. The curves for $b_a=\pm 1$, under case (iii) was another example of the symmetry.

This completes the coverage of all types of stress-strain states encountered as b_a is cycled between $\pm\hat{b}_a$, $(\hat{b}_a\geqslant 1)$, including the initial stage of virgin flux penetration. Field cycles with $\hat{b}_a<1$, or minor field loops not centered around $b_a=0$, can be analyzed in a similar manner.

V. MAGNETOSTRICTION, $\Delta R/R$

The dilatation of the cylinder diameter, or $\Delta R/R$, is an important quantity because it can be measured experimentally. Its hysteretic critical-state behavior can be calculated generally from Eq. (17). However, this is not necessary here since $\Delta R/R$ also equals the hoop strain at $\rho=1$ for which expressions are already derived. For completeness, we list the expressions for the various branches making up a full magnetostriction loop. For the virgin increasing field branch, $b_a<1$, one finds

$$\frac{\Delta R}{R}=-e_0\frac{1-\nu}{12}(6b_a^2-4b_a^3+b_a^4). \tag{50}$$

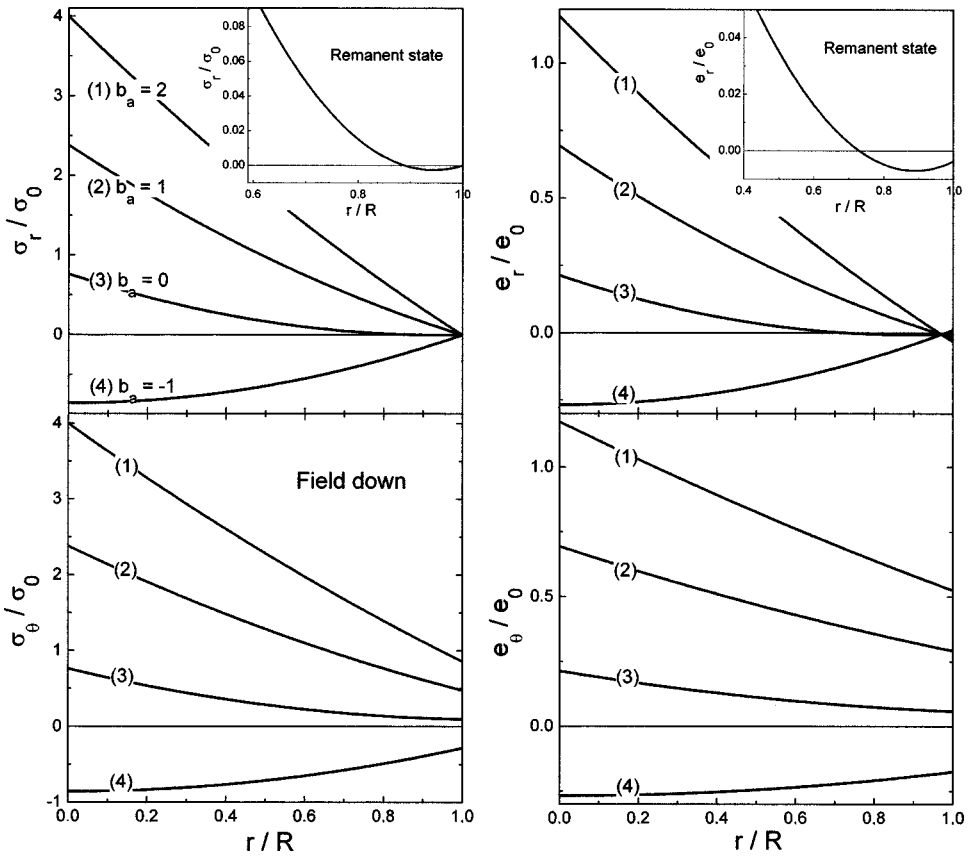

FIG. 10. Stress and strain as the field is decreased from $b_a=2$ to $b_a=-1$. Remagnetization is assumed already complete. Insets: magnification of the radial stress and strain near the edge for $b_a=0$.

At the smallest fields the radius contracts with an amount increasing as b_a^2. For $b_a \geqslant 1$ one has

$$\frac{\Delta R}{R}=e_0\frac{1-\nu}{12}(1-4b_a), \tag{51}$$

showing a linear dependence on the applied field.

As b_a starts to decrease from a maximum $\hat{b}_a$, the dilatation becomes

$$\frac{\Delta R}{R}=e_0\frac{1-\nu}{12}\left[1+4b_a-4(\hat{b}_a+b_a)\left(1-\frac{\hat{b}_a-b_a}{2}\right)^3\right]. \tag{52}$$

This expression holds until the field has been reduced to $\hat{b}_a-2$, where a further field reduction gives the magnetostriction

$$\frac{\Delta R}{R}=e_0\frac{1-\nu}{12}(1+4b_a). \tag{53}$$

The field cycle is completed using that any $\Delta R/R$ hysteresis loop must have mirror symmetry about the vertical axis. Figure 11 shows $\Delta R/R$ for b_a cycled with amplitudes $\hat{b}_a=1$, 2, and 4. Recalling that $\Delta R/R$ is proportional to the axial strain, Eq. (20), the expressions above also apply to the longitudinal dilatation if one replaces the factor $1-\nu$ by -2ν.

When $\hat{b}_a>2$ there is a part of the loop where the ascending and descending field branches are linear. The vertical width of the loop in this field range can be expressed as

$$\left.\frac{\Delta R}{R}\right|_{\downarrow}-\left.\frac{\Delta R}{R}\right|_{\uparrow}=\frac{1-\nu}{E}(\Delta MB)_a, \tag{54}$$

where $\Delta M=2Rj_c/3$ is the width of the Bean model magnetization loop. This relation allows one to make use of dilatation data in the same way as one analyzes magnetization curves to gain information about the irreversible flux behavior.[5,12] Note, however, that the simple relation is not easily generalized to other geometries, such as, e.g., long prismatic bodies. Here the magnetostrictive behavior is expected to be much more complex because of the discontinuity lines in the flow pattern of the critical current.[7]

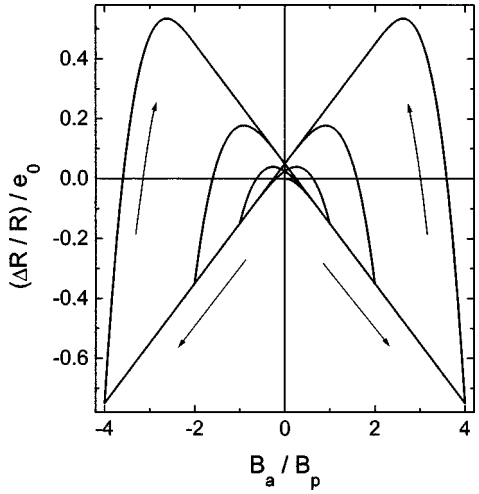

FIG. 11. Hysteretic behavior of the magnetostriction $\Delta R/R$ as the field is cycled between $\pm\hat{b}_a$ with $\hat{b}_a=1$, 2, and 4.

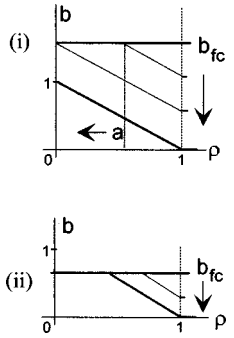

FIG. 12. Flux density profiles during field descent to the remanent state after cooling in the field b_{fc}. Shown are two situations, (i) and (ii), with b_{fc} larger and smaller than the full penetration field.

VI. FIELD COOLING

The pinning-induced stress generated by reducing the field after field cooling has been considered earlier in Ref. 4. Nevertheless it is worthwhile to consider the same process here since the previous treatment was based on the plane stress approximation, and also because the authors did not perform a complete stress distribution analysis. One should also keep in mind here the importance of field cooling as method to activate trapped-field magnets. It requires less applied fields as compared to the field-cycle method discussed in the first part of this paper. On the other hand, in the latter case the activation can be accomplished more easily using only a short high-field pulse.

Let B_{fc} denote the external field applied during the cooling. We assume that B_{fc} also is the flux density frozen in the superconductor when the subsequent field descent starts. As illustrated in Fig. 12, there are here two different situations to be considered, namely (i) $b_{fc}>1$ and (ii) $b_{fc}\leqslant 1$, where only the first gives maximum trapped field.

In both cases, field reduction implies that j_c starts to flow in an outer region, $a\leqslant\rho\leqslant 1$ where now

$$a=1-b_{fc}+b_a. \tag{55}$$

Here the flux density equals $b=b_a+1-\rho$, while in the inner part, $0\leqslant\rho<a$, the original field remains frozen, $b=b_{fc}$. The stress calculation using Eqs. (12) and (13) gives now the result for $0\leqslant\rho<a$:

$$\frac{\sigma_r}{\sigma_0}=\frac{\sigma_\theta}{\sigma_0}=b_{fc}^2-b_a^2-\frac{1-2\nu}{12(1-\nu)}(b_{fc}-b_a)^2(b_a^2+4b_a+2b_ab_{fc}+8b_{fc}-3b_{fc}^2), \tag{56}$$

and for $a\leqslant\rho\leqslant 1$:

$$\frac{\sigma_r}{\sigma_0}=(1-\rho)\left[\frac{8(2-\nu)b_a+7-2\nu}{12(1-\nu)}-\frac{3-2\nu}{1-\nu}\frac{\rho}{4}-\frac{1-2\nu}{1-\nu}\frac{3b_{fc}+b_a+1}{12}(b_{fc}-b_a-1)^3\frac{1+\rho}{\rho^2}\right], \tag{57}$$

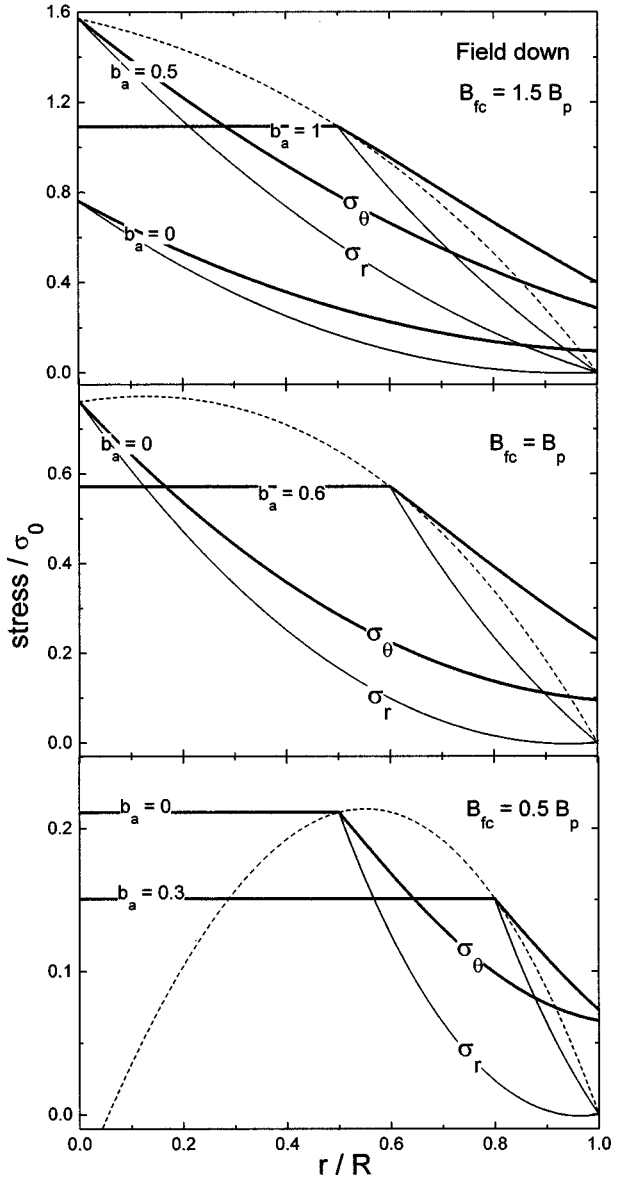

FIG. 13. Stress profiles during field descent to the remanent state after field cooling with $b_{fc}=1.5$, 1.0, and 0.5. Thick lines show σ_θ, fine lines show σ_r and dashed lines show the stress value at the magnetization front $\rho=a$.

$$\frac{\sigma_\theta}{\sigma_0}=\frac{(3+6\nu)\rho^2-8(1+\nu)(1+b_a)\rho+8(2-\nu)\hat{b}_a+7-2\nu}{12(1-\nu)}+\frac{1-2\nu}{1-\nu}\frac{3b_{fc}+b_a+1}{12}(b_{fc}-b_a-1)^3\left(1+\frac{1}{\rho^2}\right). \tag{58}$$

These formulas apply to both case (i) and (ii), although in case (i) only to the point where $b_a=b_{fc}-1$. The final descent to $b_a=0$ goes via states already discussed in Sec. IV B, and the expressions listed there hold also here. Formulas for the strain components can be derived similarly from Eqs. (18) and (19).

Figure 13 shows examples of stress profiles as b_a decreases to zero from $b_{fc}=1.5$, 1, and 0.5. The stresses are tensile and with σ_θ (bold line) always larger than or equal to σ_r (fine line). The two stress components have the same

maximum value, which one finds as plateaus in the region where the original frozen flux remains unchanged. A tiny negative σ_r exists near the surface in the remanent states.

In the upper panel, where $b_{fc}=1.5$, one sees that the plateau value steadily increases as b_a is swept down. At $b_a=b_{fc}-1$ a maximum stress of 1.56 σ_0 is reached at $\rho=0$. Upon further field reduction from $b_a=0.5$ to the remanent state, both stresses decay gradually, while being always largest in the cylinder center.

The panel in the middel, with $b_{fc}=1$, shows similar behavior except that the vanishing of the plateau now coincides with reaching the remanent state. Note from the dashed curve, indicating the stress at the magnetization front, $\rho=a$, that even here the overall stress maximum occurs before coming to the final state. Hence in this case the highest stress is experienced by a larger portion of the cylinder, namely for all $\rho\leqslant 0.13$. One can show that when

$$b_{fc}\geqslant(4-2\nu)/3, \tag{59}$$

which for our $\nu=0.3$ becomes $b_{fc}\geqslant 1.13$, the highest stress occurs only in the cylinder center, whereas for smaller b_{fc} it is experienced by an extended region.

The lower panel is included to illustrate the case (ii) of Fig. 13. Reducing here the field from $b_{fc}=0.5$ to $b_a=0$, a large inner part, $\rho<0.5$, holds the highest remanent stress.

By comparing the three panels, one sees that also here there is a strong dependence of the maximum stress on the field. In particular, one may compare the remanent states after field reduction from $b_{fc}\leqslant 1$. The stress in the central region is then from Eq. (56) given by

$$\frac{\sigma_r}{\sigma_0}=\frac{\sigma_\theta}{\sigma_0}=b_{fc}^2\left(1-\frac{1-2\nu}{1-\nu}\,\frac{8b_{fc}-3b_{fc}^2}{12}\right), \tag{60}$$

reflecting again the generally quadratic dependence on the applied field. At this point we can also compare with a formula derived in Ref. 4. Their Eq. (12), can be rewritten as the above equation with the only difference being the factor containing the Poisson ratio, which in their formula becomes $(1-\nu)$. Such deviations are typical between the plane stress and the plane strain solutions.

VII. COMPARISON OF MAXIMUM STRESS

Of prime practical importance is the overall maximum tensile stress generated as the applied field is reduced from some maximum value and down to zero. Evidently, the overall maximum stress, and also *where* it occurs in the cylinder, depends on the exact route towards the remanent state. Shown in Fig. 14 are the overall highest stress generated during field descent after field cooling and during a field cycle after zero-field cooling. The horisontal axis gives the maximum field applied in the process, i.e., b_{fc} and $\hat{b}_a$ in the field-cooling and zero-field-cooling case, respectively. Each of the three graphs is divided in two segments, one full line and one dashed, to indicate that the stress maximum differs in its location depending on the maximum applied field. The stress can be either (1) restricted to $\rho=0$, (2) distributed over an extended region near the center, or (3) restricted to some point with $\rho>0$. Shown together with the graphs are the dividing lines pointing out where each of these cases apply.

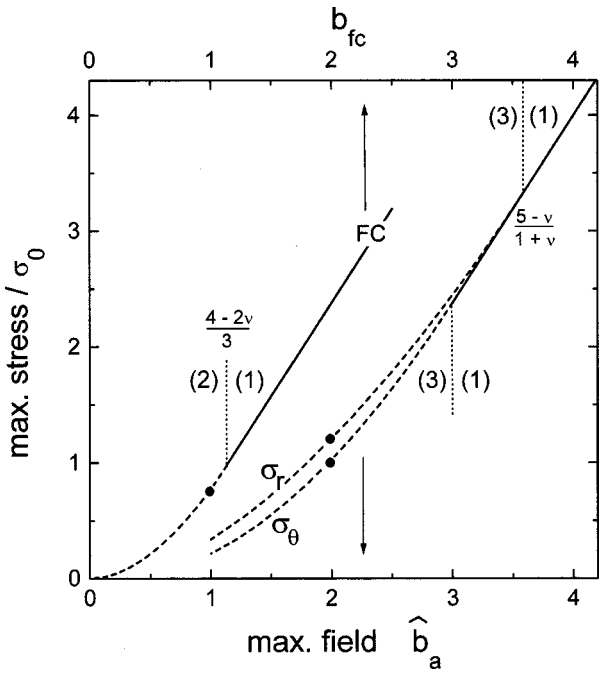

FIG. 14. Overall maximum tensile stress occurring in the cylinder during field descent to the remanent state in the field cooling (FC) and zero-field-cooling route. The stresses are plotted as functions of the maximum field, b_{fc} and $\hat{b}_a$. Regions marked by (1), (3), and (2) indicate if the corresponding stress maximum is located at $\rho=0$, at some finite ρ, or in some extended inner part of the cylinder, respectively.

Full lines always correspond to case (1).

For the field-cooling route (graph labeled FC) there is only one curve since both stress components have equal maximum values. For $b_{fc}\geqslant(4-2\nu)/3$ the highest stress increases with b_{fc} according to the linear relation

$$\frac{\sigma^{\max}}{\sigma_0}=\frac{2}{3}\,\frac{2-\nu}{1-\nu}\,b_{fc}+\frac{3-2\nu}{4(1-\nu)}, \tag{61}$$

and occurs at $\rho=0$. For the smaller b_{fc}, drawn as dashed line indicating case (2) above, the stress depends on b_{bf} in a nonlinear way resembling a parabola. Under optimum conditions for making a fully activated trapped-field magnet, i.e., using $b_{fc}=1$, the highest stress encountered is equal to $0.774\sigma_0$. This point, which is marked by a filled circle on the graph, takes place when $b_a=0.127$.

The other two curves show the overall maximum of σ_τ and σ_θ occurring in the field cycle following zero-field cooling. For large $\hat{b}_a$ the stress maxima are also here equal for both components, and take place at $\rho=0$. Their magnitude is given by

$$\frac{\sigma^{\max}}{\sigma_0}=\frac{2}{3}\,\frac{2-\nu}{1-\nu}\,\hat{b}_a+\frac{25-14\nu}{12(1-\nu)} \tag{62}$$

for $\hat{b}_a$ down to $(5-\nu)/(1+\nu)$ and 3 for the radial and hoop stress, respectively. For the smaller fields, shown as dashed curves, the maximum radial stress always lies above the hoop stress. As discussed in Sec. IV A, these stress maxima are cusped and located at some finite ρ. The highest stress occurring for the optimum condition for activating trapped-

field magnets, $\hat{b}_a = 2$, is also here indicated by filled circles. These stresses are of magnitude $\sigma_r = 1.21\sigma_0$ and $\sigma_\theta = 1.03\sigma_0$, and occur when $b_a = 0.84$ and $b_a = 0.64$, respectively. When comparing those numbers with the peak stress $0.774\,\sigma_0$ in the field-cooling route, it is clear that the latter method is strongly preferable if cracking is a real potential problem.

VIII. CONCLUSION

A full three-dimensional elasticity analysis of the flux-pinning-induced stress-strain problem has been presented. The plane strain approach was used to find an exact consistent solution for a long circular cylinder with free surfaces placed in a parallel magnetic field. By assuming a critical-state-model type of magnetic behavior the body force in the cylinder is proportional to the gradient in the flux density squared, which allows simple analytical expressions for stress and strain to be found. While the result for the external radial magnetostriction $\Delta R/R$ turned out to be the same as found earlier in a two-dimensional plane stress treatment, the present spatial distributions of stress and strain are given by different formulas. Several relations between $\Delta R/R$ and other characteristic strains were also found; both the radial and hoop strain at $r = R$, and the uniform longitudinal (axial) strain are proportional to $\Delta R/R$. The derived results are all general in the sense that stress-strain calculations can be carried out for any critical-state model $j_c = j_c(B)$.

The stress-strain behavior in the Bean model was discussed in detail for two common magnetization processes: (1) a full cycle of the applied magnetic field after zero-field cooling and (2) a field reduction to zero after field cooling. Greatest attention received the descending field stages, where the pinning-induced body forces point outwards creating tensile stress in the cylinder. Knowing the magnitude and location of the maximum tensile stress is imperative to understand and hopefully control the well-known tendency of bulk superconductors to crack up either partly or completely during magnetization with fields of several Tesla. We were able to map out the overall highest stresses in both of the magnetization processes for various maximum applied fields in process (1), and for various cooling fields in process (2). Extending the present analysis to more realistic $j_c(B)$ is under preparation.

ACKNOWLEDGMENTS

The author is grateful to J. Lothe, Y. Galperin, H. Fujimoto, and E. H. Brandt for encouragement and helpful discussions. The financial support from The Research Council of Norway is acknowledged.

[1] M. Murakami, N. Sakai, T. Higuchi, and S. I. Yoo, Supercond. Sci. Technol. **9**, 1015 (1996); A. Das, M. R. Koblischka, N. Sakai, M. Muralidhar, S. Koishikawa, T. Fukuzaki, S. J. Seo, and M. Murakami, *ibid.* **11**, 1283 (1998).

[2] M. Muralidhar, H. S. Chauhan, T. Saitoh, K. Segawa, K. Kamada, and M. Murakami, Supercond. Sci. Technol. **10**, 663 (1997).

[3] G. Fuchs, G. Krabbes, P. Schtzle, P. Stoye, T. Steiger, and K.-H. Muller, Physica C **268**, 115 (1996); H. Fujimoto, H. Kamijo, S. I. Yoo, and M. Murakami (unpublished).

[4] Y. Ren, R. Weinstein, J. Liu, R. P. Sawh, and C. Foster, Physica C **251**, 15 (1995).

[5] H. Ikuta, N. Hirota, Y. Nakayama, K. Kishio, and K. Kitazawa, Phys. Rev. Lett. **70**, 2166 (1993).

[6] H. Ikuta, K. Kishio, and K. Kitazawa, J. Appl. Phys. **76**, 4776 (1994).

[7] T. H. Johansen, J. Lothe, and H. Bratsberg, Phys. Rev. Lett. **80**, 4757 (1998).

[8] T. H. Johansen, H. Bratsberg, and J. Lothe, Supercond. Sci. Technol. **11**, 1186 (1998).

[9] S. Timoshenko and J. N. Goodier, *Theory of Elasticity* (McGraw-Hill, New York, 1951).

[10] T. H. Johansen, Phys. Rev. B **59** 11 187 (1999).

[11] A. Goyal, W. C. Oliver, P. D. Funkenbusch, D. M. Kroeger, and S. J. Burns, Physica C **183**, 221 (1991).

[12] K. Fülber, A. Geerkens, S. Ewert, and K. Winzer, Physica C **299**, 1 (1998); N. Nabialek, H. Szymczak, V. A. Sirenko, and A. I. D'yashenko, J. Appl. Phys. **84**, 3770 (1998).